ENGINEERING JOURNAL

Article

XDEM for Tuning Lumped Models of Thermochemical Processes Involving Materials in the Powder State

Edoardo Copertaro[1,*], Paolo Chiariotti[1], Alvaro A. Estupinan Donoso[2], Nicola Paone[1], Bernhard Peters[2], and Gian Marco Revel[1],

1 Dipartimento di Ingegneria Industriale e Scienze Matematiche, Università Politecnica delle Marche, Ancona, Italy
2 Faculté des Sciences, de la Technologie et de la Communication, Université du Luxembourg, Luxembourg, Luxembourg
*E-mail: e.copertaro@pm.univpm.it

Abstract. Processes involving materials in gaseous and powder states cannot be modelled without coupling interactions between the two states. XDEM (Extended Discrete Element Method) is a valid tool for tackling this issue, since it allows a coupled CFD-DEM simulation to be run. Such strength, however, mainly finds in long computational times its main drawback. This aspect is indeed critical in several applications, since a long computational time is in contrast with the increasing demand for predictive tools that can provide fast and accurate results in order to be used in new monitoring and control strategies.

This paper focuses on the use of the XDEM framework as a tool for fine tuning a lumped representation of the non-isothermal decarbonation of a $CaCO_3$ sample in powder state. The tuning of the lumped model is performed exploiting the multi-objective optimization capability of genetic algorithms.

Results demonstrate that such approach makes it possible to estimate fast and accurate models to be used, for instance, in the fields of virtual sensing and predictive control.

Keywords: Extended discrete element method, computational fluid dynamics, discrete element method, lumped element modelling, multi-objective model optimization, virtual sensing.

1. Introduction

Several engineering fields have started demanding numerical models that are able to reproduce a physical process in a fast and accurate way. This aspect is being enhanced particularly in monitoring and control applications, where these models are more and more often used to overcome either technical limits which make impractical the use of standard sensors, or to develop new feed-forward control strategies.

Virtual sensors [1] belong to the first category. In virtual sensing direct measurements on some process variables are replaced by model-based estimations from other variables that are measured in a direct way. Virtual sensing is a promising strategy, which has started to be successfully applied also in real industrial processes [2], and is particularly relevant whenever direct sensing of process variables is unfeasible because of technical or economical reasons.

Feed-forward control is a model-based control strategy where predictive models are used to anticipate disturbances before they result in a deviation of the process [3–5].

Virtual sensing and feed-forward control are up-to-date research topics, and they both require predictive models which should ensure: a) high accuracy in the representation of a process behavior (in a virtual sensor the approximations introduced by a model directly affect the measurement uncertainty); b) short computational times.

High accuracy and short computational times are requirements that can be hardly satisfied by the same model, especially when a complex physical system is addressed. This is the case of processes involving powders: for the intrinsic characteristics of a material in that state a high level of accuracy on its description can be achieved only by DEM (Discrete Element Method) models, where each particle is tracked through all its history according to a Lagrangian approach. These models, which can involve up to millions of particles and are often coupled to CFD (Computational Fluid Dynamics) models, do require both extremely long computational times and computational capacities generally available only in computer clusters. With this in mind, it is clear how such models cannot be directly used as virtual sensors nor in feed-forward control strategies.

However, an interesting approach is to use such complex modeling techniques to fine tune simplified models that could constitute the core of either virtual sensors or feed-forward control strategies.

This paper aims at discussing the use of a combined CFD-DEM approach based on the Extended Discrete Element Method (XDEM) framework [6–14], for tuning a simplified lumped model describing a decarbonation process that involves a $CaCO_3$ sample in powder state under non-isothermal conditions. The XDEM simulation associated to such process has been already validated by the authors in [15] on the basis of experimental data documented by Gieorgieva et al. [16].

The tuning of the lumped model by the XDEM simulation is performed by adopting a multi-objective optimization strategy based on genetic algorithms. The comparison between results of the two models, when applied to a test involving a higher number of particles with respect to the one reported in [15], shows how the tuned lumped model can provide a high level of accuracy with less computational effort, thus making it suitable both for virtual sensing and feed-forward control strategies.

The paper is organized as follows: the test case and the XDEM model used for tuning the lumped model are described in section II; the lumped model and the optimization strategy adopted are discussed in section III; results comparing performances of the two approaches are presented in section IV; section V draws the main conclusions of the work.

2. XDEM Representation of the CaCO3 Decarbonation Process

2.1. Experimental Setup

The experimental setup reproduced by the XDEM framework and the lumped model is the one presented by Gieorgieva et al. in [16], where small samples of powder $CaCO_3$ of about 5 ± 0.1 mg are loaded without pressing into an open platinum crucible (diameter: 6 mm; height: 3 mm). Thermogravimetrical (TG) measurements are carried out in a flow of nitrogen (N_2, 99.999 %) at a rate of 25 cm^3/min under non-isothermal conditions. The gas flow comes from the bottom of a pipe (diameter: 10 mm; length: 20 mm); the crucible is placed in the middle of the pipe. An electrical furnace provides controlled heating of the samples up to 1000 °C, at 4 different rates: 3, 6, 9, 12 K/min. During the heating process, the sample undergoes decarbonation, and a consequent mass loss occurs:

$$CaCO_3 \rightarrow CaO + CO_2 \quad (1)$$

A graphical representation of the TG furnace is shown in Fig. 1:

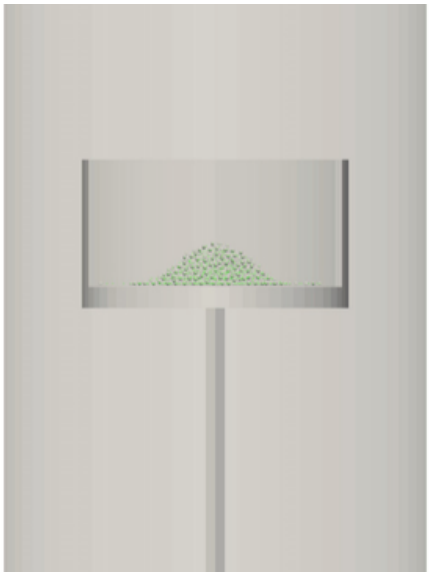

Fig. 1. Scheme of the TG furnace.

2.2. The XDEM Framework

The CFD-DEM model was developed by using the XDEM framework, a tool that makes it possible the combination of an Eulerian approach for the gas phase with a Lagrangian approach for the powder phase.

The XDEM framework uses a CFD approach for the description of the gas phase, which is consequently modeled according to equations deduced from the Navier-Stokes ones (i.e. conservation of mass, momentum and energy).

A Lagrangian approach based on DPM (Discrete Particle Method) is used for the description of the powder phase. In DPM each particle is modelled both in its dynamics and chemical conversion. However, predictions of solely motion or chemical conversion in a decoupled mode are also applicable.

2.2.1. DEM approach for the powder phase

In DPM-conversion, a discrete particle is considered to be composed of different phases: solid, inert (i.e. a solid phase that does not undergo chemical reactions), liquid, and gaseous, with the gaseous phase occupying the porous volume inside the particle. A set of one-dimensional and transient differential equations is associated to each particle, describing heat and mass transports along the radial direction *r*. These equations account for:

- Mass conservation for a generic i^{th} specie:

$$\frac{\partial \rho_i}{\partial t} = \sum_k M_i \cdot \Omega_{k,i} \quad (2)$$

$$\frac{\partial}{\partial t}\left(\epsilon_p \cdot \rho_i\right) + \frac{1}{r^2}\frac{\partial}{\partial r}\left(r^2 \cdot \rho_i \cdot v_g\right) = \frac{1}{r^2}\frac{\partial}{\partial r}\left(r^2 \cdot D_i \cdot \epsilon_p \frac{\partial \rho_i}{\partial r}\right) + \epsilon_p \cdot \sum_k M_i \cdot \Omega_{k,i} \quad (3)$$

with Eq. (2) and (3) valid for solid/liquid and gaseous species, respectively. The porosity of the particle, i.e. the fraction of void space respect to the total volume, is represented by the ϵ_p term; v_g is the velocity of the gas phase and Ω_k is the production or consumption rate consequent to the k^{th} chemical conversion. The terms ρ_i, D_i and M_i represent the mass density, the diffusion coefficient

and the molar mass of the i^{th} specie, respectively. Based on the conservation of mass for the different species, the porosity of the particles is evaluated as a function of r.

- Conservation of linear momentum:

$$-\frac{\partial p_g}{\partial r} = \frac{\mu_g \cdot \epsilon_p}{K_p} \cdot v_g \tag{4}$$

being p_g the pressure of the gas phase, μ_g its viscosity and K_p the so-called permeability characterizing the morphology of the porous particle.

- Conservation of energy:

$$\frac{\partial(\rho_p \cdot c_p \cdot T_p)}{\partial t} = \frac{1}{r^2}\frac{\partial}{\partial r}\left(r^2 \cdot \lambda_{eff} \cdot \frac{\partial T_p}{\partial r}\right) + \sum_k \Omega_k \cdot H_k \tag{5}$$

where ρ_p, c_p and T_p are, respectively, the mass density, the specific heat and the temperature of the particle. The term λ_{eff} is the effective thermal conductivity whose calculation is described in [17] and H_k is the enthalpy of the k^{th} reaction.

2.2.2. CFD approach for the gas phase

The CFD domain is described on a coarser level respect to the individual channels of the tortuous void spaces inside the packed bed of particles. This averaged representation is obtained by defining a Representative Elementary Volume (REV). The linear dimension of the REV, L_{REV}, should respect the following condition:

$$L_g \ll L_{REV} \ll L \tag{6}$$

being L the characteristic length of the problem and L_G the microscopic dimension associated with the voids inside the packed bed (in the present case L_{REV} is assumed 10 times bigger respect to the diameter of the particles). All the thermo-physical and chemical properties of the CFD domain are averaged inside the REVs (<> symbol). The Navier-Stokes equations are derived from a model developed for flows through a packed bed characterized by the global porosity ε_f. These equations are reported hereafter.

- Conservation of mass for a generic i^{th} specie:

$$\frac{\partial}{\partial t}\left(\epsilon_f \cdot \langle \rho_{f,i} \rangle\right) + \nabla \cdot \left(\epsilon_f \cdot \langle \rho_{f,i} \rangle \cdot \langle \vec{v}_f \rangle\right) = \langle \dot{m}_{f,i} \rangle \tag{7}$$

being $\rho_{f,i}$ the mass density of the i^{th} specie, $\vec{v}_f$ the velocity field and $\dot{m}_{f,i}$ a source/sink term that accounts for mass transfers between the CFD domain and the particles.

- Conservation of momentum:

$$\begin{aligned} &\frac{\partial}{\partial t}\left(\epsilon_f \cdot \langle \rho_f \rangle \cdot \langle \vec{v}_f \rangle\right) + \nabla \cdot \left(\epsilon_f \cdot \langle \rho_f \rangle \cdot \langle \vec{v}_f \rangle \times \langle \vec{v}_f \rangle\right) \\ &= \nabla \cdot \left(\epsilon_f \cdot \langle \vec{\tau}_f \rangle\right) - \frac{\mu_f}{K_{bed}} \epsilon_f^2 \cdot \langle \vec{v}_f \rangle - C_{bed} \cdot \langle \rho_f \rangle \cdot \epsilon_f^3 \cdot |\langle \vec{v}_f \rangle| \cdot \langle \vec{v}_f \rangle \end{aligned} \tag{8}$$

In Eq. (8), τ_f denotes the deviatoric component of the stress tensor and μ_f represents the viscosity of the CFD gas. K_{bed} and C_{bed} are empirical terms which are calculated according to the geometrical characteristics of the packed bed and the flow regime. Their expressions are reported hereafter (D_p denotes the particles diameter):

$$K_{bed} = \frac{D_p^2 \cdot \epsilon_f^3}{150 \cdot (1-\epsilon_f)^2} \quad (9)$$

$$C_{bed} = \frac{1.75 \cdot (1-\epsilon_f)}{D_p \cdot \epsilon_f^3} \quad (10)$$

- Conservation of energy:

$$\frac{\partial}{\partial t}(\epsilon_f \cdot \langle \rho_f \rangle \cdot \langle h_f \rangle) + \nabla \cdot (\epsilon_f \cdot \langle \rho_f \rangle \cdot \langle h_f \rangle \cdot \langle \vec{v}_f \rangle) = \frac{\partial \langle p_f \rangle}{\partial t} + \langle \vec{v}_f \rangle \cdot \nabla \langle p_f \rangle + \langle \dot{q}_f \rangle \quad (11)$$

being h_f the enthalpy of the CFD gas, p_f the pressure and $\dot{q}_f$ a source/sink term which accounts for heat transfers between the CFD gas and the particles.

2.2.3. CFD–DEM coupling

Heat transfer and mass transfer for a gaseous i^{th} specie between the CFD gas and the particles are calculated according to Eq. (12) and Eq. (13), respectively:

$$\langle \dot{q}_f \rangle = \sum_{j=1}^{N} \frac{A_j}{V_{REV}} \cdot \alpha \cdot \left(T_{p,j} - \langle T_f \rangle\right) \quad (12)$$

$$\langle \dot{m}_{f,i} \rangle = \sum_{j=1}^{N} \frac{A_j}{V_{REV}} \cdot \beta_i \cdot \left(\rho_{p,i,j} - \langle \rho_{f,i} \rangle\right) \quad (13)$$

being N the total number of particles comprised inside a REV and A the surface area of the particle. The coefficients α and β_i are the heat and mass transfer coefficients, whose expressions are functions of the Nusselt and Sherwood numbers of the CFD domain. These heat and mass transfers are included into the Navier-Stokes equations as source/sink terms, whilst they provide the boundary conditions to Eq. (3) and (5) for each particle, as stated in the following:

$$-\lambda_{eff} \cdot \left.\frac{\partial T_p}{\partial r}\right|_{r=R_p} = \alpha \cdot \left(T_p - T_f\right) + \dot{q}_{cond} + \dot{q}_{rad} \quad (14)$$

$$-D_i \cdot \left.\frac{\partial \rho_{p,i}}{\partial r}\right|_{r=R_p} = \beta_i \cdot \left(\rho_{p,i} - \rho_{f,i}\right) \quad (15)$$

The R_p term represents the radius of the particle. The terms $\dot{q}_{cond}$ and $\dot{q}_{rad}$ respectively account for conductive and radiative heat transfers with all the neighbor particles comprised inside a cutoff distance. Their expressions for a generic i^{th} particle are reported in Eq. (16) and in Eq. (17):

$$\dot{q}_{i,cond} = \sum_{j=1}^{N} A_{c,ij} \cdot \frac{1}{\frac{1}{\lambda_i} + \frac{1}{\lambda_j}} \cdot \frac{T_{p,i} - T_{p,j}}{\Delta x_{ij}} \quad (16)$$

$$\dot{q}_{i,rad} = \sum_{j=1}^{M} V_{(i \to j)} \cdot \epsilon \cdot \sigma \cdot \left(T_{p,i}^4 - T_{p,j}^4\right) \quad (17)$$

In the former equations σ represents the Stefan-Boltzmann constant, ε the emissivity, N and M are the number of particles comprised inside the respective cutoff distances for conduction and radiation. The contact area A_c is assumed to be quadratic, and linearly dependent on the particles overlap [18]. The view factor V is calculated as the ratio between the surface area of the i^{th} particle and the sum of the surface areas of the M neighbors.

2.3. CFD-DEM Model

The experimental setup was reproduced using the XDEM framework. A total number of 1000 spherical particles (constant diameter of 7.8e-5 m) have been placed inside the furnace at the bottom of the crucible (Fig. 1). These particles provide a total mass of 5 mg. Positions of the particles have been obtained by running the dynamic module of DPM, which uses a Hertz/Coulomb model for calculating the reciprocal mechanical interactions. The dynamic simulation is a highly time consuming one, because the proper contact detection requires extremely reduced time steps (1e-4 s in the present case). Particles positions have

been therefore calculated once, before running the conversion simulation. The sample is assumed static during the whole TG process, even if particles weight changes (this assumption is not expected to introduce relevant errors in the representation of the conversion process).

Particles are characterized by an initial porosity ε_p of 0.1. The initial composition of the solid phase is 100 % $CaCO_3$, whilst the porous volume is filled with pure N_2, i.e. the gas flowing inside the TG furnace. The continuous flow of N_2 removes the gaseous products of decarbonation (CO_2). This holding, and considering the inert characteristic of N_2, conversion of $CaCO_3$ into CaO is assumed to be irreversible. The conversion rates associated to the process are reported hereafter:

$$\Omega_{CaCO_3} = -k \cdot C_{CaCO_3} \tag{18}$$

$$\Omega_{CaO} = k \cdot \frac{M_{CaO}}{M_{CaCO_3}} \cdot C_{CaCO_3} \tag{19}$$

$$\Omega_{CO_2} = k \cdot \frac{M_{CO_2}}{M_{CaCO_3}} \cdot C_{CaCO_3} \tag{20}$$

In Eq. (18) to (20), *C* denotes the molar concentration. The rate constant *k* is expressed according to an Arrhenius formulation: the pre-exponential factor and activation energy are taken from the experimental results of Gieorgieva (7.41e16min^{-1} and 325.1 kJ/mol, respectively).

During the TG test, particles constituting the sample are heated by convection from the gas of the CFD domain. Heat is redistributed inside the sample, by conduction and radiation. As decarbonation is activated, the solid phase of the particles starts converting into CaO: as a consequence, the porosity changes and CO_2 is released into the void spaces. Then, CO_2 is convoyed out of the particles, by a combination of advective and diffusive transport mechanisms. The N_2 flow of the CFD domain continuously removes the CO_2 expelled from the particles. A validation of the model discussed so far is reported in [15].

3. Simplified Lumped Model

The thermo-chemical phenomena involved during the TG experiments were also analyzed by developing a lumped model of the process. Such model is based on the following three Ordinary Differential Equations (ODEs):

$$\mathrm{c_{pw} \cdot m_w \frac{dT_w}{dt} = A_c \cdot h_1 \cdot (T_g - T_w) + A_c \cdot \sigma \cdot \varepsilon \cdot (T_g^4 - T_w^4) + h_2 \cdot A_b \cdot (T_s - T_w)} \tag{21}$$

$$\mathrm{c_{ps} \cdot m_s \cdot \frac{dT_s}{dt} = h_2 \cdot A_b \cdot (T_w^4 - T_s^4) + m_s \cdot C \cdot k \cdot \Delta H} \tag{22}$$

$$\mathrm{\frac{dC}{dt} = k \cdot C} \tag{23}$$

For a better understanding of the symbols used in Eq. (21), (22) and (23), the reader is invited to look at the "Nomenclature" section of the paper.

The heat balance over the crucible (Eq. (21)) accounts for convective and radiative heat exchanges between the gas and the crucible, and for conductive heat exchange between the crucible and the sample. The heat balance over the sample (Eq. (22)) accounts for conductive heat exchange with the crucible and heat absorbed by the decarbonation process. The mass balance equation (Eq. (23)) describes the decreasing of $CaCO_3$ mass fraction during decarbonation. The reaction constant *k* of Eq. (23) is a function of the sample temperature, and varies according to the Arrhenius formulation reported hereafter:

$$\mathrm{k = A \cdot e^{\frac{-E}{R \cdot T_s}}} \tag{24}$$

In Eq. (24), *A* is the pre-exponential factor, *E* the activation energy and *R* the gas constant.

In Eq. (21), the gas temperature T_g varies according to Eq. (25), where *hr* represents the heating rate of the experiment and *t* the time base:

$$\mathrm{T_g = 293.15 + hr \cdot t} \tag{25}$$

The model identified by the former equations can be graphically reproduced exploiting a Thermal-Electrical Analogy (Fig. 2).

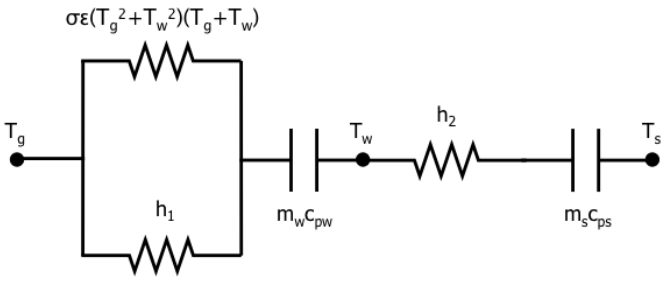

Fig. 2. Thermal-electrical analogy.

A precise evaluation of the conductive heat exchange coefficient between the crucible and the sample (h_2) and the pre-exponential constant (A) in the Arrhenius equation is difficult and experimental data available in literature exhibit large uncertainty. Literature [19, 20] reports values widely ranging between 50 and 150 W/(m²K) for the heat exchange coefficient between a powder material and solid wall (h_2). The kinetic of a reaction involving a material in powder state is deeply affected by the shape properties of the particles, like the free surface: this introduces high uncertainty in the estimation of the pre-exponential factor A of Eq. (24).

On the other hand, the detailed framework of equations constituting the XDEM approach is effective in providing a precise description of the local phenomena at particle scale: in this sense, the conductive heat transfer with the crucible is calculated for each individual particle, by computing the correspondent contact area. At the same way, the definition of specific physical properties for each particle (instantaneous porosity, free surface, etc.) makes it possible to address the conversion process at a great level of detail, going into the local particle scale.

For these reasons, the aforementioned CFD-DEM model was used to tune the h_2 and A parameters of the lumped model. Such tuning requires the minimization of two main variables: the errors associated with the estimations of the mean temperature and the mass loss of the sample over time. This multi-objective optimization problem was solved using a genetic algorithm (GA) approach [21, 22] and considering the objective functions reported in Eq. (26) and (27).

$$Obj_1 = \sum_i \left(\frac{T_{i,XDEM} - T_{i,lumped}}{T_{i,XDEM}} \right)^2 \tag{26}$$

$$Obj_2 = \sum_i \left(\frac{w_{i,XDEM} - w_{i,lumped}}{w_{i,XDEM}} \right)^2 \tag{27}$$

In the former equations, $T_{i,XDEM}$ and $T_{i,lumped}$, and $w_{i,XDEM}$ and $w_{i,lumped}$ represent, respectively, the sample mean temperature and mass loss predictions by XDEM and the lumped model at an i^{th} time step during a heating process at 15 K/min (the mean temperature esteemed from XDEM is calculated as the average temperature of the whole particles constituting the sample).

The pre-exponential factor A was varied in a ± 50 % range relative to the nominal value (7.41e16 min^{-1}) indicated by Gieorgieva in [16]. The h_2 coefficient was varied in the range 50-150 W/(m²K) as indicated in [19, 20]. The genetic algorithm was run with an initial population size set to 30. After 120 iterations the optimization led to the Pareto frontier, i.e. the set of the solutions that cannot be improved in any of the objectives without degrading at least one of the other objectives, shown in Fig. 3.

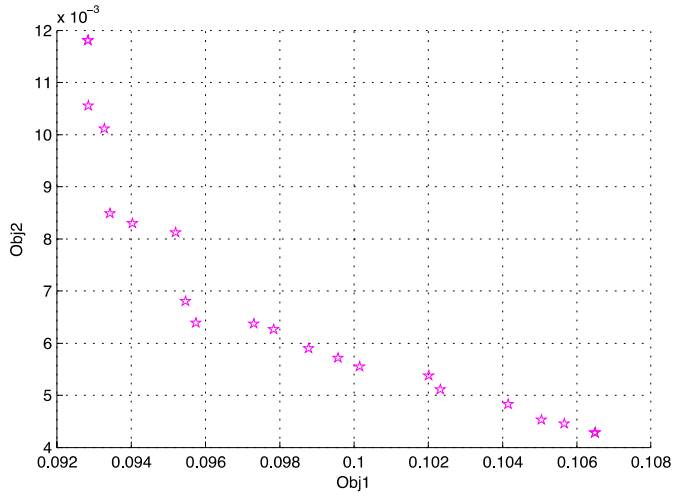

Fig. 3. Pareto frontier obtained by the GA optimization.

Among all solutions belonging to the Pareto frontier, it was decided to choose the one minimizing Obj_2, which corresponds to an h_2 coefficient equal to 73.5 W/(m²K) and an A coefficient equal to 1.63 s^{-1}. Mass loss is indeed the variable mainly representing the reaction. Therefore, by ensuring minimization of Obj_2, the correct behavior of the whole reaction is guaranteed.

Figure 4 shows a comparison between predictions from XDEM and the lumped model for the sample mean temperature during the thermogravimetric analysis (the slight underestimation of temperature from the lumped element model is due to the specific heat capacity, which is assumed constant and not calculated according to the instantaneous mass fractions). An analogous comparison regarding the sample mass loss is presented in Fig. 5. The average mean relative error is in the order of 2 %. Computational time moves from days-basis for the CFD-DEM model, if run on a single workstation with more than 30 cores, to 1.3 s on an Intel I5 core laptop (non-compiled version).

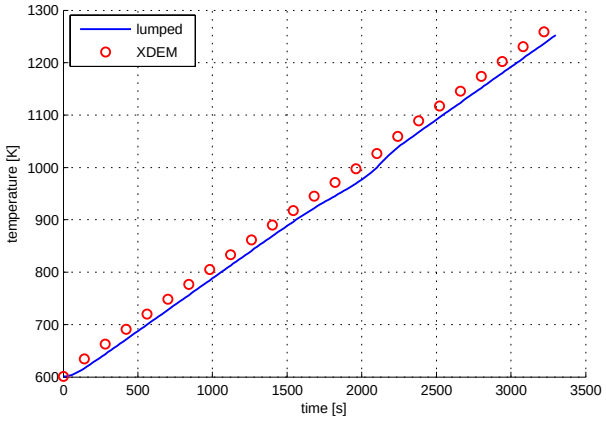

Fig. 4. Sample mean temperature estimates from XDEM and the lumped model during the thermogravimetric analysis.

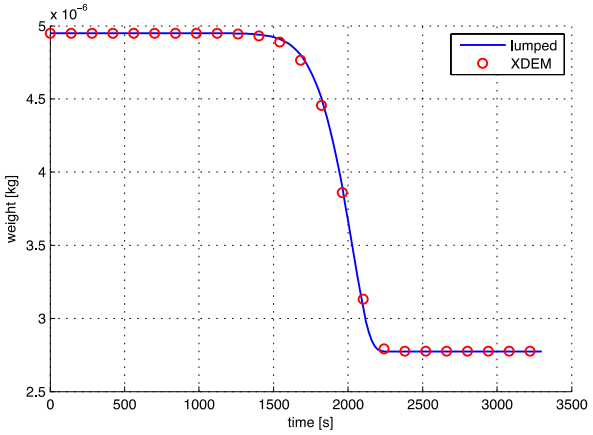

Fig. 5. Sample mass loss estimates from XDEM and the lumped model during the termogravimetric analysis.

4. Results

In order to check the correctness of the previous optimization step and the consequent capability of the lumped model to provide consistent results for different working conditions, XDEM was used to create reference results. A thermogravimetric analysis with varied input parameters was simulated, mainly varying the total mass of the sample, 10 mg, and consequently the number of particles (moved from 1000 to 2000), and the heating rate (6 K/min) to get the sample from room temperature up to 1000 °C. Table 1 reports the XDEM main parameters.

Table 1. XDEM main simulation parameters.

Gas Volumetric flow	25 cm^3/min
N2 weight fraction in gas	99.9999 %
Sample total mass	10 mg
Particles radius	7.8e-5 m
Initial porosity	0.1
Number of particles	2000
CaCO3 initial weight fraction	100 %
Pre-exp. Factor	7.41e16 min^{-1}
Activation energy	325.1 kJ/mol
Crucible height	3 mm
Crucible diameter	6 mm
Temperature range	20-1000 °C
Heating rate	6 K/min

Figure 6 shows the streamlines of the CFD domain inside the TG furnace. The gas flow originates from the bottom of the crucible, forms a toroidal vortex and then forms a plum that flows along the crucible axis in the vertical direction, reaching the top. The two vortex rings inside the crucible enhance the heat transfer with the sample and facilitate the removal of the gaseous CO_2 that is produced by the particles during the decarbonation.

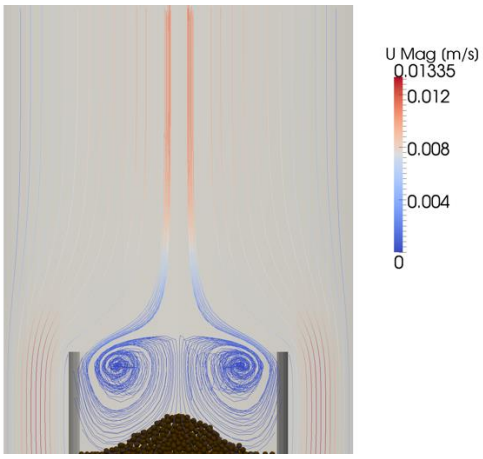

Fig. 6. Streamlines of the CFD domain.

Figures 7 to 9 show the CO_2 mass fraction in the CFD domain at three different times: when the instantaneous temperature activates decarbonation, at the time when the conversion rate reaches a maximum and when the reaction is completed. CO_2 mass fraction inside the sample reaches a maximum at 7600 s, then, when reaction is completed, CO_2 mass fraction decreases because of the continuous flow of N_2 coming from the bottom of the pipe: therefore, N_2 removes CO_2 from the crucible.

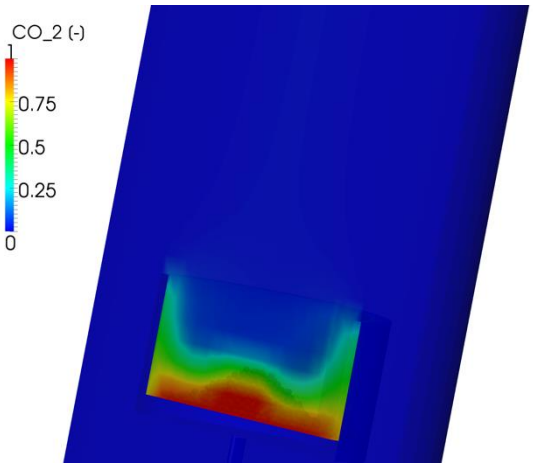

Fig. 7. CO_2 mass fraction at t=7000 s.

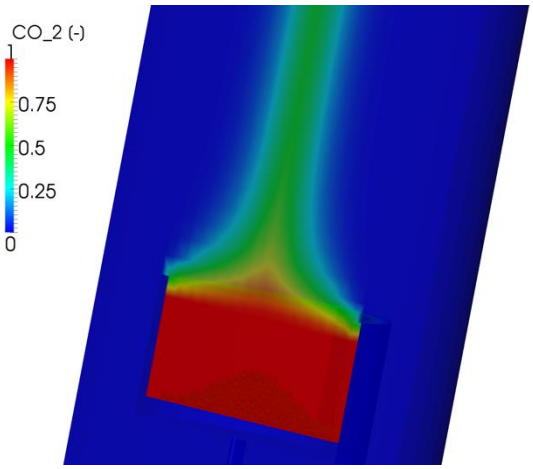

Fig. 8. CO_2 mass fraction at t=7600 s.

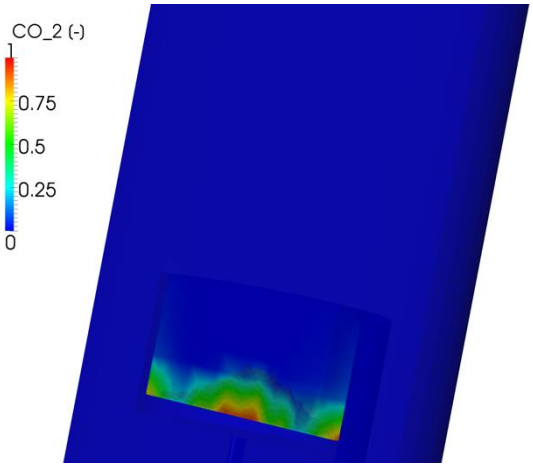

Fig. 9. CO_2 mass fraction at t=8000 s.

As a consequence of the temperature distribution, decarbonation starts earlier in the particles at the bottom of the sample, as it can be noted in Fig. 10. The early reaction on these particles is evident in Fig. 11 and Fig. 12, where $CaCO_3$ and CaO masses for each particle inside the sample while reaction is progressing are reported.

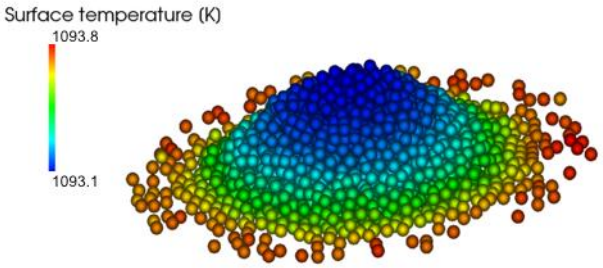

Fig. 10. Temperature distribution of the sample at t=9000 s.

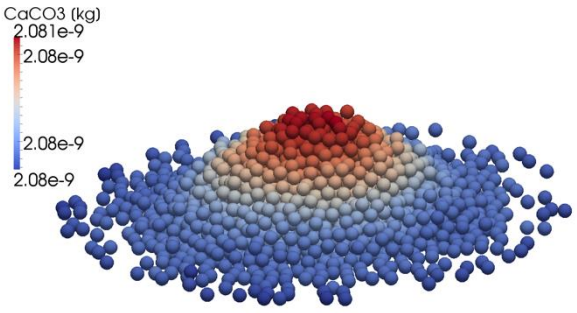

Fig. 11. $CaCO_3$ mass for each particle of the sample at t=7600 s.

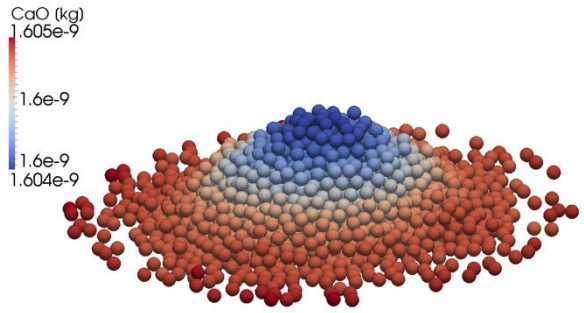

Fig. 12. CaO mass for each particle of the sample at t=7600 s.

Previous results proved XDEM capability of providing a detailed and accurate representation of the whole phenomena involved during a TG analysis. The combined Eulerian-Lagrangian approach joins the capability of providing an exhaustive representation of the field variables of the gas domain with the possibility of tracking every single particle overt time.

The lumped model was then tested using such new input parameters: m_s was adjusted according to the new mass of the sample, br was updated to the new heating rate, whilst the A and b_2 coefficients were kept fixed to the values obtained by the optimization step. Figures 13 and 14 report a comparison between estimates of sample mean temperature and mass loss provided by XDEM and the lumped model.

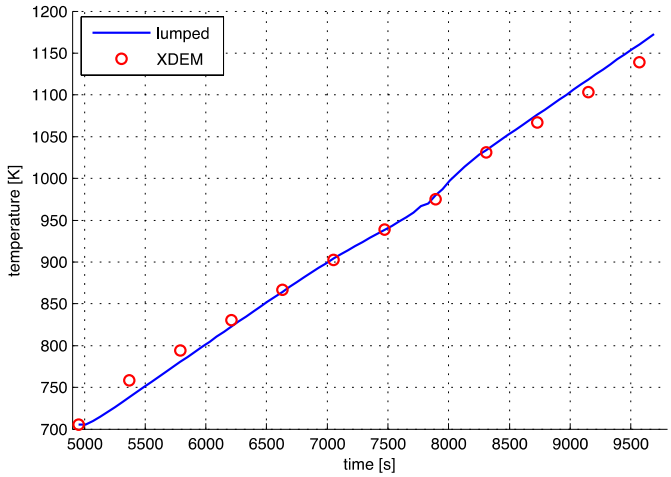

Fig. 13. Estimations from XDEM and the lumped model for the mean temperature of the sample during the TG analysis.

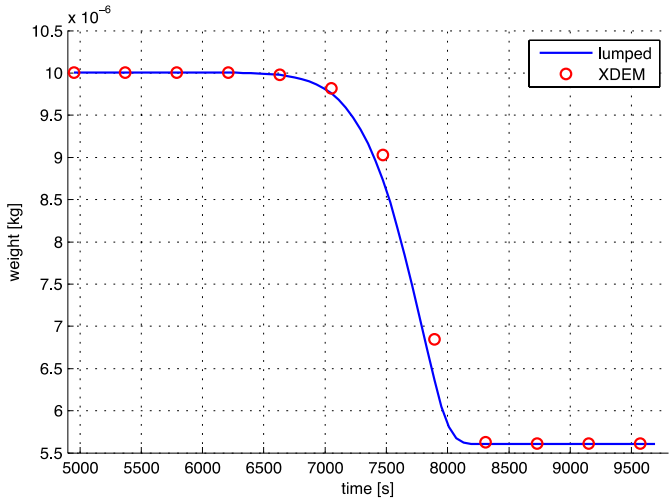

Fig. 14. Estimations from XDEM and the lumped model for the weight loss of the sample during the TG analysis.

An average error in the order of 1% can be noted between the two sets of predictions.

5. Conclusions

This paper shows the capability of the XDEM framework to provide realistic and reliable predictions of thermal and chemical phenomena taking place in processes that involve both a gas phase and materials in powder state.

Furthermore, it demonstrates how extremely complex and time-consuming CFD-DEM models could be well exploited to fine tune simplified models aiming at providing accurate solutions in drastically reduced computational times.

Indeed, the $CaCO_3$ decarbonation process described by Georgieva can be well approximated by the lumped model developed, once the model has run into a tuning process involving XDEM. The genetic algorithm-based multi-objective optimization step resulted to be a good actor for performing such tuning operation.

The final accuracy of the lumped model, 1% with respect to the CFD-DEM model, shows the potentials of such approach whenever a direct tuning operation is not possible because of the impossibility of getting reliable data to work on (e.g. impossibility of direct measurements, high uncertainty associated to literature data, etc.).

6. Nomenclature

XDEM framework:

	Symbols
ρ	Mass density
M	Molar mass
Ω	Reaction rate
ε	Porosity (emissivity when specified)
r	Radius
v	Velocity
D	Diffusion coefficient
p	Pressure
μ	Viscosity
c_p	Specific heat
T	Temperature
λ	Thermal conductivity

H	Enthalpy
A	Surface area
Ac	Contact area
σ	Stefan-Boltzmann constant
k	Reaction constant
C	Molar concentration
Subscripts	
p	Particle
g	Gas phase inside the particles
f	Gas of the CFD domain

Lumped model:

T_w	Temperature of the crucible
T_s	Temperature of the sample
T_g	Temperature of the gas phase
C	Weight fraction of $CaCO_3$
h_1	Heat exchange coefficient between gas and crucible
h_2	Heat exchange coefficient between sample and crucible
c_{pw}	Specific heat of the crucible
c_{ps}	Specific heat of the sample
m_w	Mass of the crucible
m_s	Mass of the sample
A_c	External area of the crucible
A_b	Bottom area of the crucible
σ	Stefan-Boltzmann constant
ε	Emissivity of the crucible
k	Rate constant of the reaction of decarbonation
H	Enthalpy of the reaction of decarbonation
A	Pre-exponential factor
E	Activation energy
R	Gas constant
hr	Heating Rate of the experiment
t	Time base

7. References

[1] P. Kadlex, B. Gabrys, and S. Strandt, "Data-driven soft sensors in the process industry," *Comput. Chem. Eng*, vol. 33, pp. 795-814, 2009.

[2] J. W. Cheng, T. Chao, L. Chang, and B. Huang, "A model-based virtual sensing approach for the injection molding process," *Polymer Engineering and Science*, vol. 44, pp. 1605-1614, 2004.

[3] A. G. Abilov, Z. Zeybek, O. Tuzunalp, and Z. Telatar, "Fuzzy temperature control of industrial refineries furnaces through combined feedforward/feedback multivariable cascade systems," *Chemical Engineering and Processing*, vol. 41, pp. 87-98, 2002.

[4] M. Fallahpour, A. Fetehi, B. N. Araabi, and M. Azizi, "A neuro-fuzzy controller for rotary cement kilns," in *17th World Congress The International Federation of Automatic Control*, Seoul, Korea, 2008.

[5] R. Kumar, S. K. Singla, and V. Chopra, "Comparison among some well known control schemes with different tuning methods," *Journal of Applied Research and Technology*, vol. 13, pp. 409-415, 2015.

[6] A. A. Estupinan Donoso and B. Peters, "XDEM employed to predict reduction of tungsten oxide in a dry hydrogen atmosphere," *International Journal of Refractory Metals and Hard Materials*, vol. 49, pp. 88-94, 2015.

[7] A. A. Estupinan Donoso, F. Hoffmann, and B. Peters, "Extended discrete element method used for convective heat transfer predictions," *Int. Rev. Mech. Eng*, vol. 7, pp. 328-336, 2013.

[8] B. Peters, X. Besseron, A. A. Estupinan Donoso, F. Hoffmann, M. Michael, and A. Mahmoudi, "The extended discrete element method (XDEM) applied to drying of a packed bed," *Journal of the International Research Foundation*, 2014.
[9] A. H. Mahmoudi, F. Hoffmann, and B. Peters, "Application of XDEM as a novel approach to predict drying of a packed bed," *Int. J. Therm. Sci.*, vol. 75, pp. 65-75, 2014.
[10] B. Peters, "Validation of a numerical approach to model pyrolysis of biomass and assessment of kinetic data," *Fuel*, vol. 90, pp. 2301–2314, 2011.
[11] B. Peters, "Prediction of pyrolysis of pistachio shells based on its components hemicellulose, cellulose and lignin," *Fuel Process. Technol.*, vol. 92, pp. 1993–1998, 2011.
[12] B. Peters, "Applying a detailed reaction mechanism to pyrolysis of *Miscanthus giganteus*," *J. Appl. Anal. Pyrol.*, vol. 91, pp. 352–358, 2011.
[13] F. Hoffmann and B. Peters, "An integrated approach to model blast furnaces," in *4th International Conference on Modelling and Simulation of Metallurgical Processes in Steelmaking*, Dusseldorf, Germany, 2011.
[14] F. Hoffmann and B. Peters, "Extended discrete element method (XDEM) to model heterogeneous reactions in packed beds," in *International Congress on Particle Technology*, Nuremberg, Germany, 2013.
[15] E. Copertaro, P. Chiariotti, A. A. Estupinan Donoso, N. Paone, B. Peters, and G. M. Revel, "A discrete-continuous approach to describe $CaCO_3$ decarbonation in non-steady thermal conditions," *Powder Technology*, vol. 275, pp. 131-138, 2015.
[16] V. Gieorgieva, L. Vlaev, and K. Gyurova, "Non-isothermal degradation kinetics of $CaCO_3$ from different origin," *Journal of Chemistry*, 2013.
[17] F. Hoffmann, "Modelling heterogeneous reactions in packed beds and its application to the upper shaft of a blast furnace," Ph.D. thesis, Université du Luxembourg, 2014.
[18] B. Peters, *Thermal Conversion of Solid Fuels*. WIT Press, 2013.
[19] P. Gorog, "Heat transfer in direct-fired rotary kilns," Ph.D. thesis, Michigan Technological University, 1977.
[20] R. K. Shah, "Laminar flow friction and forced convection heat transfer in ducts of arbitrary geometry," *International Journal of Heat and Mass transfer*, vol.18, pp. 849-862, 1975.
[21] K. Deb, *Multi-Objective Optimization Using Evolutionary Algorithms*. John Wiley & Sons, 2001.
[22] H. Mühlenbein, M. Schomisch, and J. Born, "The parallel genetic algorithm as function optimizer," *Parallel computing*, vol. 17, pp. 619-632, 1991.